EPJ Web of Conferences **371**, 01021 (2026) https://doi.org/10.1051/epjconf/202637101021
AMT'2026

SADI numerical solution of the heat transfer by Hartmann laminar flow inside a channel subjected to a constant temperature

Mahmoud Dargal[1*], *Hassan* Ait Kazite[1], *Abdelaziz* Oubarra[1], and *Khalid* Zniber[1]

[1]Department of Physics, Faculty of Sciences Ain Chok, Hassan II University, Km 8 El Jadida Road, Maarif, P.O. Box 5366, Casablanca, Morocco

Abstract. This work investigates the thermal behavior of a fluid flowing in a planar channel whose outer walls are kept at a fixed temperature while being exposed to a homogeneous magnetic field. The primary purpose is to examine how the governing parameters affect both the thermal distribution and the Nusselt number. For this purpose, a generalized Graetz-type problem is considered by including the influence of a magnetic field applied perpendicular to the flow direction, together with viscous dissipation, Joule heating, and axial heat conduction. The numerical treatment is carried out using the Splines Alternating Direction Implicit (SADI) technique. One of the main advantages of this approach is its ability to compute spatial gradient terms directly without relying on classical finite-difference approximations, which improves the accuracy of gradient boundary conditions and facilitates the treatment of complex geometries. The study also evaluates the effects of the controlling parameters on both axial and bulk temperature distributions as well as on the heat transfer characteristics represented by the Nusselt number. This methodology provides an accurate and efficient tool for simulating heat transfer phenomena in magnetohydrodynamic flows.

1 Introduction

Because of its major importance in the development of industrial thermal devices, heat transfer associated with laminar forced convection has been widely investigated. This topic is especially relevant for flows occurring inside circular ducts and channels formed by parallel plates. It is known that the presence of a magnetic field significantly affects the heat transfer mechanism by modifying the velocity distribution of the fluid or liquid metal, which consequently changes the temperature field. The relative influence of electromagnetic and viscous effects is generally represented by the Hartmann number.

*Corresponding author: mahmouddargal.o@gmail.com

Moreover, the thermal conditions imposed at the wall, whether in terms of temperature or heat flux, play a key role in many engineering applications, particularly in the conception of nuclear reactor cooling technologies and in the thermal analysis of Stirling-cycle heat exchangers.

A literature review shows that there is a significant body of work, both numerical and theoretical, dedicated to the study of this flow with imposed boundary conditions. The earliest studies in this research area were those conducted by Graetz (1883-1885), In his work, forced convective heat transfer for a fully developed laminar flow of a Newtonian fluid inside a circular tube was investigated under imposed wall temperature conditions. Assuming negligible viscous dissipation and ignoring axial thermal conduction within the fluid, Graetz obtained a reduced form of the energy equation. This formulation was later solved analytically by W. Nusselt through the method of variable separation, representing an important contribution to heat transfer theory. The pioneering study initiated by L. Graetz opened the way for numerous experimental, theoretical, and numerical studies devoted to more realistic situations involving complex geometries, relaxed assumptions, and non-Newtonian fluid behavior.

J. Lahjomri et al. [1] investigated the thermal behavior and enhanced Nusselt number in the thermal entrance region of laminar magnetohydrodynamic (MHD) flow between two parallel plates. Their model incorporated viscous dissipation, Joule heating, and axial heat conduction together with gradually varying wall temperatures. In addition, they developed an asymptotic solution for the modified Mathieu equation. The study revealed that when (B_r \neq 0), the Nusselt number rises with the Hartmann number for electrically insulating walls, whereas it decreases for perfectly conducting walls as the Hartmann number increases. Iboud-Saouli et al. [2] examined entropy generation in an electrically conducting fluid flowing between two uniformly heated parallel plates under a transverse magnetic field. Their findings demonstrated that stronger magnetic effects increase the fluid temperature because of magnetic dissipation and consequently lead to higher entropy generation. KVS Raju et al. [3] analyzed steady MHD forced convection of a viscous fluid with finite depth through a saturated porous medium inside a horizontal channel. The lower wall of the channel was considered impermeable and thermally insulated. Their formulation included both viscous dissipation and Joule heating effects. Selcuk Selimli et al. [4] numerically investigated the influence of magnetic fields on steady laminar flow inside a liquid lithium channel. Their work focused mainly on the magnetic impact on the flow characteristics. Michiyoshi and Matsumoto [5] studied laminar heat transfer in a parallel-plate channel exposed to a transverse magnetic field in two semi-infinite zones. In their analysis, viscous dissipation and axial conduction were neglected, while the electrical circuit was assumed open with zero net current. J. Lahjomri et al. [6] derived an analytical solution to the extended Graetz problem in the presence of a transverse magnetic field with an imposed uniform wall heat flux. Their approach assumed a uniform inlet temperature and incorporated internal heat generation in the energy equation. K. Zniber et al. [7] presented an analytical investigation of laminar MHD flow in a two-dimensional channel subjected to a constant magnetic field. The channel walls were heated along the entire length using a sinusoidal heat flux with either zero or non-zero mean value. Using the linear operator method, the authors obtained expressions for the temperature field together with local and average Nusselt numbers. Joule heating and viscous dissipation were neglected, whereas axial conduction effects were considered. Mohamed Eissa Sayed Ahmed [8] introduced a finite-difference numerical approach to examine heat transfer and power-law fluid flow in a rectangular duct influenced by a magnetic field. Haroun Ragueb et al. [9] investigated heat transfer and entropy generation in an MHD microchannel under differential heating conditions while accounting for viscous dissipation and Joule heating.

A fully implicit finite-difference scheme was applied to predict temperature distribution and entropy production accurately. Elalaoui et al. [10] analyzed laminar heat transfer in the thermal entrance region of a corrugated conduit subjected to a constant wall heat flux. Kumar et al. [11] explored entropy generation and heat transfer in a micropolar nanofluid flowing through a porous microchannel under magnetic field effects. The Buongiorno model together with the ANOVA–Taguchi optimization technique was employed. The nonlinear equations were solved numerically using the Runge–Kutta–Fehlberg algorithm and verified through the differential transformation method. Their results showed that the Prandtl number contributes most significantly (79.73%), while increasing the material parameter lowers entropy generation and improves thermodynamic efficiency. Bhatti et al. [12] studied heat transfer in an electromagnetohydrodynamic Carreau fluid flowing between two rectangular plates. The coupled nonlinear governing equations were solved using the differential transformation method (DTM).

In the present study, unlike the investigations previously reported in the literature, the extended Graetz problem is solved under the influence of a transverse magnetic field with constant wall temperature conditions while accounting for viscous dissipation, Joule heating, and axial thermal conduction. The numerical solution is obtained using the implicit Splines Alternating Direction Implicit (SADI) method. Since this technique allows the direct evaluation of spatial derivative terms without relying on finite-difference discretization, boundary conditions involving gradients can be treated with higher accuracy. Furthermore, the current analysis assumes that the inlet temperature is not uniform, but varies as a consequence of viscous dissipation and Joule heating effects. The main objective of this work is to examine the influence of the governing parameters on the axial and bulk temperature distributions as well as on the Nusselt number.

2 Mathematical Formulation

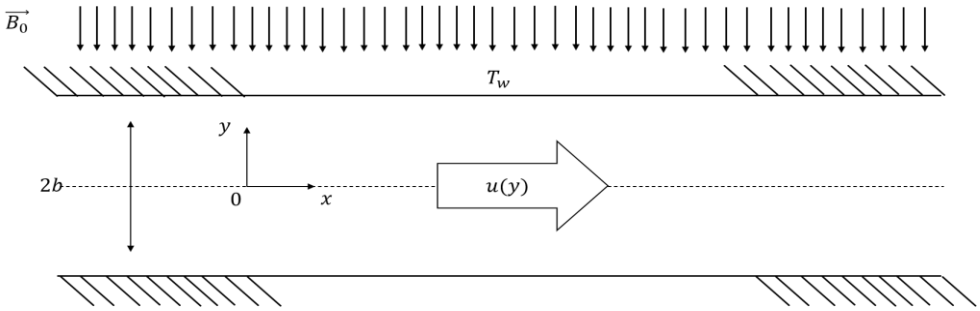

Figure 1: Problem description

Consider a conducting fluid flowing inside a horizontal channel of great length L, and height $2b$, where the walls are subjected to a uniform and constant temperature T_w , and placed in a transverse magnetic field $\overrightarrow{B_0}$ (Figure 1). In this case, the force of gravity is neglected, and the fluid motion is maintained by the pressure gradient. To facilitate the analysis of the problem, several simplifying assumptions have been adopted.

First, the fluid is assumed to be incompressible, which allows neglecting density variations. The flow is considered laminar and unidirectional, simplifying the modeling of the forces involved. The thermophysical properties of the fluid are assumed to be

constant, thereby eliminating the complexity associated with temperature and pressure variations. Additionally, heat transfer is analyzed in a two-dimensional framework, taking into account thermal gradients in two main directions. The wall is considered rigid, with a no-slip condition, implying that the fluid velocity is zero at the wall. Furthermore, the effects of viscous dissipation and Joule heating are integrated into the study to better understand internal thermal phenomena. Finally, axial conduction in the fluid is taken into account, allowing for a more realistic modeling of heat exchange along the flow.
For thermally developing flow with an already established velocity profile, the energy equation describing the temperature field in magnetohydrodynamic (MHD) flow between two parallel plates incorporates several physical phenomena. Among these are axial heat conduction, viscous dissipation, and Joule heating effects. The formulation is developed by considering the symmetry of the configuration relative to the xOz plane.

$$\rho C_P\left[\frac{\partial \mathbf{T}(x,y,t)}{\partial t}+\mathbf{u}(y)\frac{\partial \mathbf{T}(x,y,t)}{\partial x}\right]=K\left[\frac{\partial^2 \mathbf{T}(x,y,t)}{\partial x^2}+\frac{\partial^2 \mathbf{T}(x,y,t)}{\partial y^2}\right]+\sigma B_0^2\mathbf{u}^2(y)+\mu\left[\frac{\partial \mathbf{u}(y)}{\partial y}\right]^2 \quad (1)$$

The velocity profile associated with a fully established laminar magnetohydrodynamic (MHD) flow of a liquid metal is written in the following form:

$$\mathbf{u}(y)=U_m\frac{ch(H_a)-ch\left(H_a\frac{y}{b}\right)}{ch(H_a)-1} \quad (2)$$

Where U_m is the maximum velocity, and $H_a=B_0\sqrt{\frac{\sigma}{\mu}}b$ is the Hartmann number.

By introducing the following dimensionless quantities into the equations:

$$\eta=\frac{y}{b} \qquad \xi=\frac{x}{P_e b} \qquad \boldsymbol{\theta}(\xi,\eta,\tau)=\frac{T-T_i}{T_w-T_i} \qquad \mathbf{U}(\eta)=\frac{\boldsymbol{u}(y)}{U_m} \qquad \tau=\frac{\alpha t}{b^2}$$

With $P_e=\frac{U_m b\,\rho C_p}{K}$ the Peclet number, defined as the ratio of energy transferred by convection to that transferred by conduction along the flow axis.
After introducing the appropriate dimensionless variables, equation (1) can be rewritten in the following nondimensional form:

$$\frac{\partial \boldsymbol{\theta}(\xi,\eta,\tau)}{\partial \tau}+\mathbf{U}(\eta)\frac{\partial \boldsymbol{\Theta}(\xi,\eta,\tau)}{\partial \xi}=\frac{\partial^2 \boldsymbol{\Theta}(\xi,\eta,\tau)}{\partial \eta^2}+\frac{1}{Pe^2}\frac{\partial^2 \boldsymbol{\Theta}(\xi,\eta,\tau)}{\partial \xi^2}+R(\eta) \quad (3)$$

The dimensionless heat equation is:
With:

$$R(\eta)=B_r H_a^2\mathbf{U}(\eta)^2+B_r\left[\frac{\partial \mathbf{U}(\eta)}{\partial \eta}\right]^2$$

With:$B_r=\frac{\mu U_m^2}{K(T_w-T_i)}$ the Brinkman number, which represents the ratio of the energy dissipated by viscous and Joule forces to the energy transferred by thermal conduction.
Where :

$$\mathbf{U}(\eta)=\frac{ch(H_a)-ch(H_a\eta)}{ch(H_a)-1} \quad (4)$$

The boundary and initial conditions in dimensionless form are:

- Initial condition :

$$\boldsymbol{\theta}(\xi,\eta,\tau=0)=0 \tag{5}$$

➢ Boundary conditions:

- At the wall:

$$\boldsymbol{\theta}(\xi,\eta=1,\tau)=1 \qquad \forall\xi>0 \tag{6}$$

- At the outlet:

$$\left.\frac{\partial\boldsymbol{\theta}(\xi,\eta,\tau)}{\partial\xi}\right|_{\xi\to+\infty}=0 \tag{7}$$

- At the axis of symmetry:

$$\left.\frac{\partial\boldsymbol{\theta}(\xi,\eta,\tau)}{\partial\eta}\right|_{\eta=0}=0 \quad \forall\xi>0 \tag{8}$$

- At the inlet:

The conduit is divided into two parts, with the first upstream part ($\xi<0$) being thermally insulated. The objective in this region is the hydrodynamic and thermal development of the fluid. As the fluid flows, the temperature changes due to dissipation phenomena in this part, which is sufficiently long for development to ensure that at least near $\xi=0$ we have $\frac{\partial\boldsymbol{\theta}(\xi,\eta)}{\partial\xi}=K_1$ (see the appendix A for details):

$$\begin{aligned}\boldsymbol{\theta}(0,\eta)=+&\frac{\frac{ch(H_a)}{2}\eta^2-\frac{ch(H_a)}{H_a^2}}{(ch(H_a)-1)^2}K_1\\&-\frac{B_rH_a^2}{(ch(H_a)-1)^2}\left[\frac{ch(H_a)^2\eta^2}{2}-\frac{2\,ch(H_a)\,ch(H_a\eta)}{H_a^2}\right.\\&\left.-\frac{ch(H_a\eta)^2}{2H_a^2}\right]+\frac{-B_rH_a^2}{(ch(H_a)-1)^2}\left[\frac{ch(H_a)^2}{H_a^2}+\frac{ch(H_a)^2}{2H_a^2}\right]\end{aligned} \tag{9}$$

With:

$$K_1=\frac{B_r\,H_a^2\,ch(H_a)}{ch(H_a)-1} \tag{10}$$

Two important parameters commonly used in heat transfer analysis are the bulk fluid temperature T_b and the Nusselt number Nu. The Nusselt number can be defined as follows:

$$Nu = -\frac{k\left.\frac{\partial T}{\partial y}\right|_{y=b}}{T_b - T_w}\frac{4b}{k} \tag{11}$$

With:

$$\mathbf{T_b}(x) = \frac{\int_0^b \mathbf{u}(y)\mathbf{T}(x,y)dy}{\int_0^b \mathbf{u}(y)dy} \tag{12}$$

In dimensionless form, they are given by:

$$Nu(\xi) = \frac{4\left.\frac{\partial \boldsymbol{\theta}}{\partial \eta}\right|_{\eta=1}}{\boldsymbol{\theta_w}(\xi) - \boldsymbol{\theta_b}(\xi)} \tag{13}$$

With:

$$\boldsymbol{\theta_b}(\xi) = \frac{\int_0^1 \mathbf{U}(\eta)\boldsymbol{\theta}(\xi,\eta)d\eta}{\int_0^1 \mathbf{U}(\eta)d\eta} \tag{14}$$

3 Numerical Method

The cubic spline alternating direction implicit (ADI) technique involves several steps that lead to the construction of a tridiagonal algebraic system expressed in terms of the function values or their first and second derivatives at the grid nodes. The boundary conditions are determined through a general relation derived from the fundamental spline equations. We set:

$$l_{i,j} = \frac{\partial \theta}{\partial \xi} \qquad L_{i,j} = \frac{\partial^2 \theta}{\partial \xi^2}$$

$$m_{i,j} = \frac{\partial \theta}{\partial \eta} \qquad M_{i,j} = \frac{\partial^2 \theta}{\partial \eta^2}$$

From the energy equation (3), we have:

$$\frac{\theta_{i,j}^{k+1/2} - \theta_{i,j}^{k}}{\frac{\Delta\tau}{2}} + u_j l_{i,j}^{k+1/2} = \frac{1}{P_e^2} L_{i,j}^{k+1/2} + M_{i,j}^{k} + R_j \tag{15}$$

Therefore:

$$\theta_{i,j}^{k+1/2} = \theta_{i,j}^{k} - \frac{\Delta\tau}{2} u_j l_{i,j}^{k+1/2} + \frac{\Delta\tau}{2P_e^2} L_{i,j}^{k+1/2} + \frac{\Delta\tau}{2} M_{i,j}^{k} + \frac{\Delta\tau}{2} R_j \tag{16}$$

According to [13], it is found that the function $\theta_{i,j}$ can be expressed in the following form:

$$\theta_{i,j}^{k+1/2} = F_{i,j} + G_{i,j} l_{i,j}^{k+1/2} + S_{i,j} L_{i,j}^{k+1/2} \tag{17}$$

By comparison with equation (16), the coefficients $F_{i,j}$, $G_{i,j}$, $S_{i,j}$ are determined.

$$F_{i,j} = \theta_{i,j} + \frac{\Delta\tau}{2}\left[M_{i,j} + R_j\right] \tag{18}$$

$$G_{i,j} = -\frac{\Delta\tau}{2} u_j \tag{19}$$

$$S_{i,j} = \frac{\Delta\tau}{2P_e^2} \tag{20}$$

From the energy equation (3), we have:

$$\frac{\theta_{i,j}^{k+1} - \theta_{i,j}^{k+1/2}}{\frac{\Delta\tau}{2}} + u_j l_{i,j}^{k+1/2} = \frac{1}{P_e^2} L_{i,j}^{k+1/2} + M_{i,j}^{k+1} + R_j \tag{21}$$

Therefore:

$$\theta_{i,j}^{k+1} = \theta_{i,j}^{k+1/2} - \frac{\Delta\tau}{2} u_j l_{i,j}^{k+1/2} + \frac{\Delta\tau}{2P_e^2} L_{i,j}^{k+1/2} + \frac{\Delta\tau}{2} M_{i,j}^{k+1} + \frac{\Delta\tau}{2} R_j \tag{22}$$

According to [13], it is found that the function $\theta_{i,j}$ is written in the following form:

$$\theta_{i,j}^{k+1} = F'_{i,j} + G'_{i,j} m_{i,j}^{k+1} + S'_{i,j} M_{i,j}^{k+1} \tag{23}$$

By comparison with equation (22), we find:

$$F'_{i,j} = \theta_{i,j} - \frac{\Delta\tau}{2} l_{i,j} + \frac{\Delta\tau}{2P_e^2} L_{i,j} + \frac{\Delta\tau}{2} R_j \tag{24}$$

$$G'_{i,j} = 0 \tag{25}$$

$$S'_{i,j} = \frac{\Delta\tau}{2} \tag{26}$$

Determination of the coefficients $\mathbf{A(i)}, \mathbf{B(i)}, \mathbf{C(i)}, \mathbf{D(i)}, \boldsymbol{A'(j)}, \boldsymbol{B'(j)}, \boldsymbol{C'(j)}, \boldsymbol{D'(j)}$ for the first and second steps.

- For the first step:

We now aim to determine the coefficients of the ADI spline for the first step. According to [13], the solution for the first derivative is expressed in the following form:

$$A(i) l_{i-1,j}^{k+1/2} + B(i) l_{i,j}^{k+1/2} + C(i) l_{i+1,j}^{k+1/2} = D(i) \tag{27}$$

- For the second step:

We now aim to determine the coefficients of the ADI spline for the second step. According to [13], the solution for the first derivative is expressed in the following form:

$$A'(j) m_{i,j-1}^{k+1} + B'(j) m_{i,j}^{k+1} + C'(j) m_{i,j+1}^{k+1} = D'(j) \tag{28}$$

The steps of resolution:
Using the cubic spline collocation relations [13], Equation (3) can be reformulated in tridiagonal form. In the first step, we solved the tridiagonal system to obtain the coefficients $l_{i,j}$ using the Thomas algorithm. Subsequently, we determined $L_{i,j}$ through spline interpolation formulas and computed $\theta_{i,j}$ using expression (17). The second step

followed an analogous procedure: solving the tridiagonal system for $m_{i,j}$ values, then deriving $M_{i,j}$ from cubic spline relations [13], and calculating $\theta_{i,j}$ via expression (23).
Determination of the Nusselt number:
The Nusselt number expressed by equation (13) can be discretized as:

$$N_u(i) = \frac{4m_{i,N_y}}{1-\theta_b(i)} \tag{29}$$

With:

$$\theta_b(i) = \frac{\sum_{j=1}^{N_y} u_j \theta_{i,j} \Delta\eta}{\sum_{j=1}^{N_y} u_j \Delta\eta} \tag{30}$$

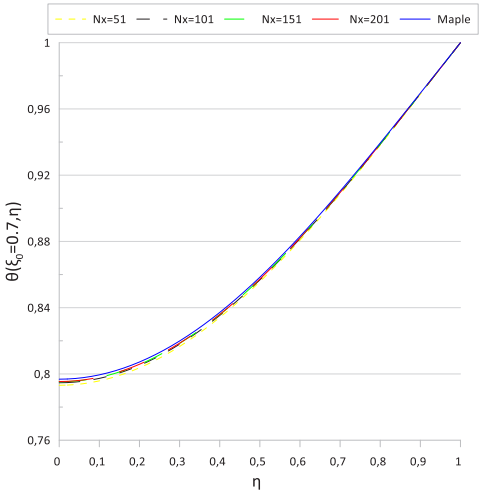

Figure 2: Radial temperature profile for different grid sizes at $H_a = 5, B_r = 0, P_e = 100$ and for $\xi_0 = 0.7$

In Figure 2 the mesh selection for grids of $51 \times 51, 101 \times 51, 151 \times 51$ and 201×51 is presented for $P_e = 100, H_a = 5$ and $B_r = 0$ at $\xi_0 = 0.7$. By comparing these curves for different grids with a solution obtained using the Maple software via the pdSolve command which solves parabolic-type differential equations we chose a value of $P_e = 100$ to neglect the effect of axial conduction. The results for the 101×51 grid agree well with those obtained for the 201×51 grid. Additionally, we observe that our steady-state solution matches perfectly with the solution obtained using Maple. Note that this steady-state regime is achieved after several iterations, the number of which depends on the chosen parameters (ranging from 100000 to 200000).

4 Results and Discussion

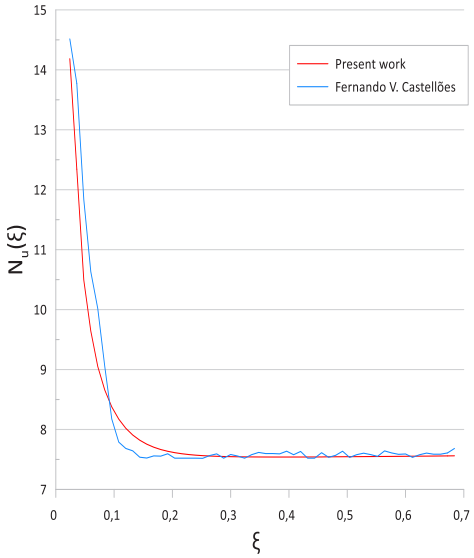

Figure 3: Comparison of the Nusselt number with the results of Fernando V. Castellões [14]

Figure 3 shows a comparison of the local Nusselt number with those obtained by Fernando V. Castellões [12] for $P_e = 10$; $B_r = 0$ and $H_a = 0.01$. It can be seen that the present results are in good agreement with those of Fernando V. Castellões. This provides additional validation for the Cubic ADI Spline method. Furthermore, for the case where H_a is greater than 5, P_e is infinite, and $B_r = 0$, this work is in agreement with the work of Lahjomri et al [1].

The Effect of $\boldsymbol{H_a}$

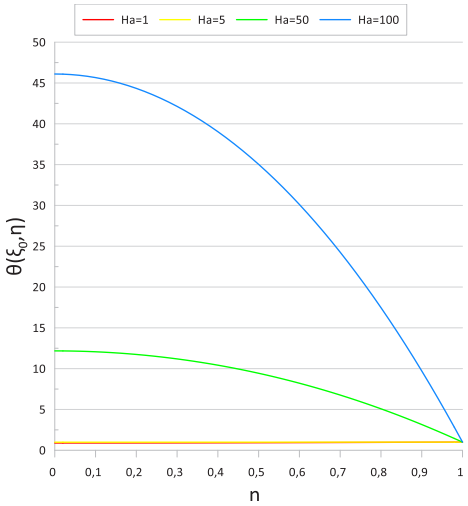

Figure 4: Radial temperature variation for different Hartmann numbers with $\xi_0 = 2.7$ $P_e = 1.5$ $B_r = 0.01$

In Figure 4 and Figure 5, the radial temperature is plotted for the cases$B_r = 0.01$ and $B_r = 0$ at $P_e = 1.5$ for four different values of the Hartmann number: $H_a = 1, 5, 50$ and

100 and $\xi_0 = 2.7$. In each figure, it is shown that the radial temperature generally maintains the same shape. In Figure 4 it is observed that the radial temperature for $\eta = 0$ reaches a maximum value higher than the wall temperature due to the non-zero value of B_r which causes heating through dissipation. The temperature decreases as η increases, eventually approaching the wall temperature at $\eta = 1$. It is also noted in Figure 4 that the radial temperature increases with an increase in the Hartmann number due to Joule heating. In Figure 5 it is observed that the radial temperature for $\eta = 0$ is lower than the wall temperature because B_r meaning there is no heating through dissipation. This value increases as η increases, eventually approaching the wall temperature at $\eta = 1$. In the same figure, it is seen that the radial temperature decreases as H_a increases up to a certain value, beyond which no further effect on the radial temperature is observed. The explanation here is that an increase in H_a slows down the fluid motion, reducing the convection velocity in the system, and thus heat transport by the fluid becomes less efficient. This results in a lower temperature distribution in the fluid away from the walls.

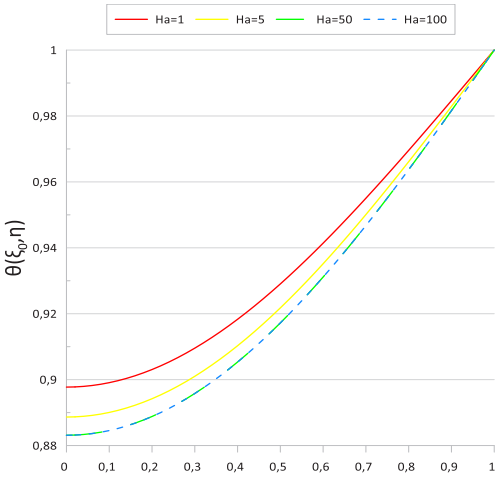

Figure 5: Radial temperature variation for different Hartmann numbers with $\xi_0 = 2.7$ $P_e = 1.5$ $B_r = 0$

In Figure 6 and Figure 7, the average temperature is plotted for the cases $B_r = 0.01$ and $B_r = 0$ at $P_e = 1.5$ for four different values of the Hartmann number: $H_a = 1, 5, 50$ and 100. In each figure, it is observed that the average temperature generally maintains the same shape. In both figures, the average temperature increases with an increase in ξ. In Figure 6 it is noted that an increase in H_a significantly raises the temperature due to Joule heating. However, in the case where $B_r = 0$ (Figure 7) H_a has a weak to negligible effect due to the absence of viscous dissipation and Joule heating, as described by equation (3) where the term responsible for temperature rise induced by these effects is canceled.

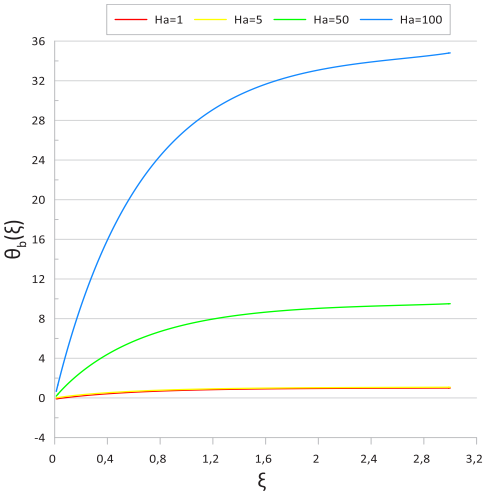

Figure 6: Mean temperature distribution for $P_e = 1.5$ $B_r = 0.01$

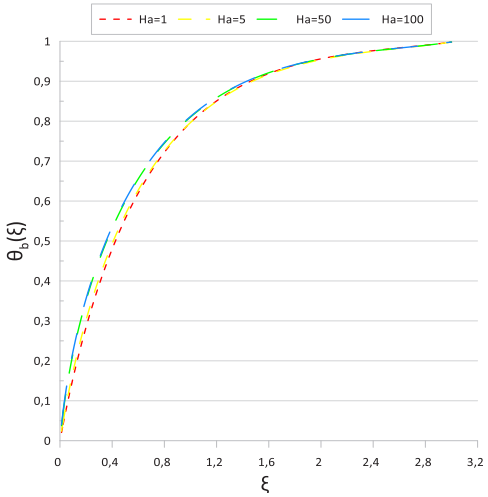

Figure 7: Mean temperature distribution for $P_e = 1.5$ $B_r = 0$

The Effect of B_r

In Figure 8 and Figure 9, the radial temperature is plotted for the cases $P_e = 1.5$ and $P_e = 100$ respectively, at $H_a = 5$ and for three different values of the Brinkman number: $B_r = 0, 0.001, 0.01$ and for $\xi_0 = 2.7$. In each figure, it is shown that the radial temperature generally maintains the same shape, except for the curve where $B_r = 0.01$ where a decrease is observed for $P_e = 100$. It is noted that over the entire interval of η from 0 to 1 the radial temperature increases with an increase in B_r due to heating through dissipation. For the same value of $B_r = 0.01$, the radial temperature in the case of $P_e = 100$ is higher than the wall temperature, unlike what is observed for $P_e = 1.5$ This is due to the increase in P_e which signifies the importance of convective heat transfer, leading

to significant heating through viscous dissipation. In Figure 10 the radial temperature is plotted for $P_e = 1.5$, $H_a = 5$ and three values of the Brinkman number: $B_r = 0, 0.001\ and\ 0.01$ at $\xi_0 = 0.3$. In this figure, it is shown that the effect of B_r is negligible due to the chosen value of ξ_0 This is further highlighted in Figure 11 which represents the average temperature for $P_e = 1.5$, $H_a = 5$ and three values of the Brinkman number: $B_r = 0, 0.001$ and 0.01 It is observed that the three curves generally maintain the same shape. As ξ increases, the average temperature also rises, and as B_r increases, the average temperature follows the same trend. However, for values of $\xi \leq 0.4$ has no effect on the average temperature because the fluid is still close to the channel entrance.

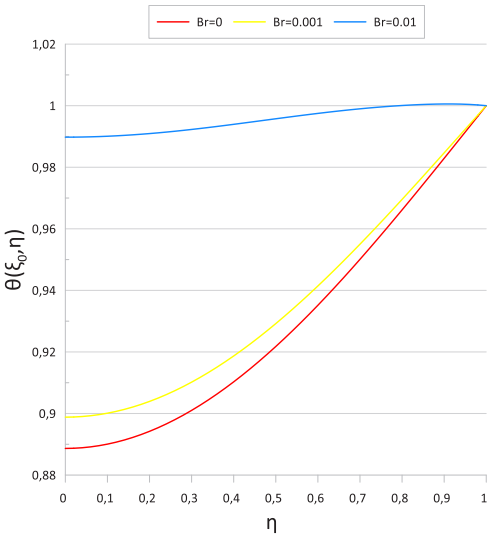

Figure 8: Radial temperature variation for different Brinkman numbers with $\xi_0 = 2.7$ $P_e = 1.5$ $H_a = 5$

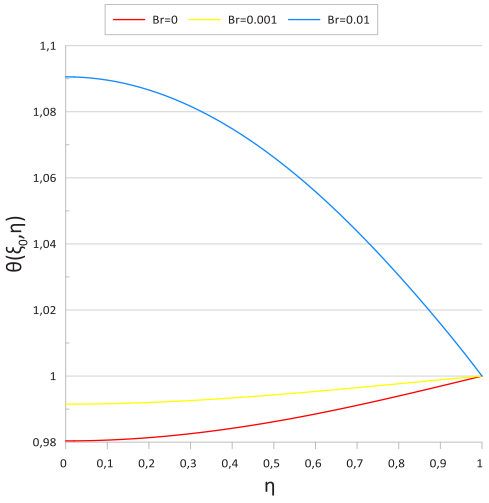

Figure 9: Radial temperature variation for different Brinkman numbers with $\xi_0 = 2.7$ $P_e = 100$ $H_a = 5$

As we move further away from this entrance, the fluid becomes increasingly heated due to dissipation, and thus the effect of B_r becomes more significant farther from the entrance.

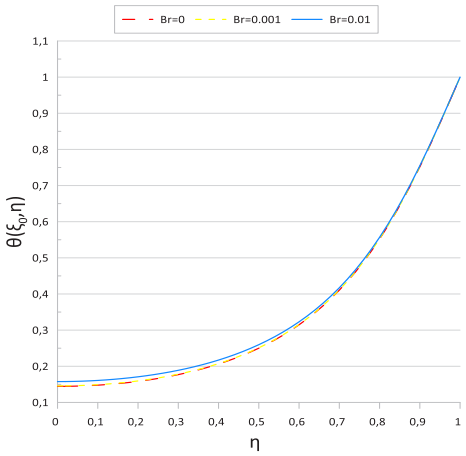

Figure 10: Radial temperature variation for different Brinkman numbers with $\xi_0 = 0.3$ $P_e = 1.5$ $H_a = 5$

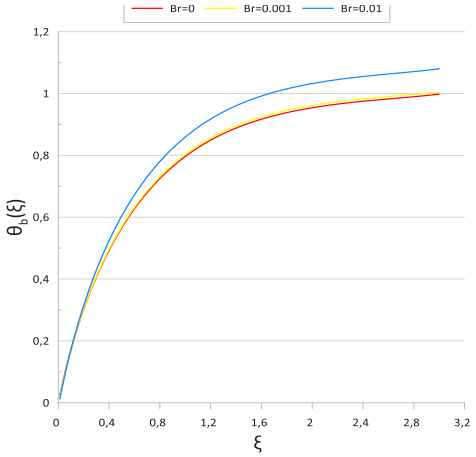

Figure 11: Mean temperature distribution for $P_e = 1.5$ $H_a = 5$

The Effect of P_e

In Figure 12, the radial temperature is plotted for $B_r = 0.001$ and $H_a = 5$, for five different values of the Peclet number: $P_e = 1.5, 10, 15, 40$ and 100, with $\xi_0 = 2.7$. It is shown that all the curves generally maintain the same shape. In this case, it is observed that the radial temperature increases with the increase in η until it approaches the value of the wall temperature. It is also noted that an increase in P_e tends to raise the temperature up to $P_e = 40$ beyond which little to no effect on the temperature profile is observed. Additionally, it is observed that the increase with η is more significant when P_e is small.

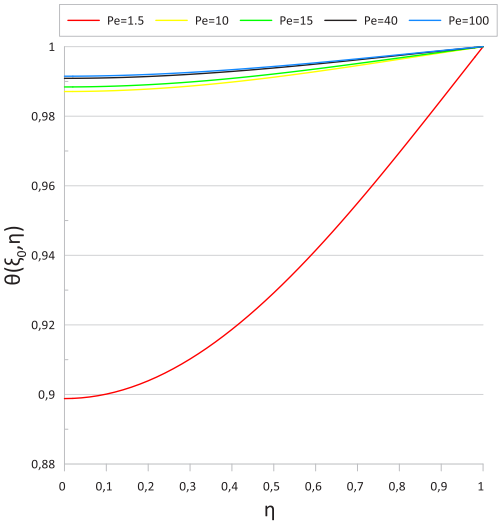

Figure 12: Radial temperature variation for different Peclet numbers with $\xi_0 = 2.7$ $H_a = 5$ $B_r = 0.001$

Figure 13 illustrates the effect of P_e on the mean temperature for $H_a = 5$ and $B_r = 0$ with five distinct values of the Peclet number: $P_e = 1.5, 10, 15, 40$ and 100. It is observed that the five curves generally maintain the same shape. The mean temperature increases with the rise in P_e until $P_e = 10$ at which point saturation is reached, meaning no further effect of P_e on the mean temperature is observed due to the neglect of axial conduction. Additionally, the asymptotic value of 1 for the mean temperature is quickly attained for larger values of P_e.

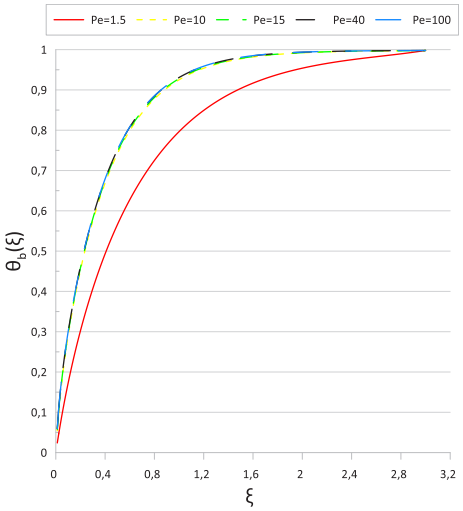

Figure 13: Mean temperature distribution for $H_a = 5$ $B_r = 0$

Nusselt Number

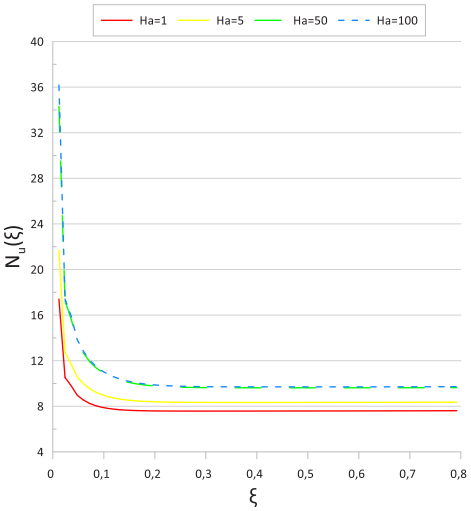

Figure 14: Distribution of local Nusselt number for $P_e = 100\ and\ B_r = 0$

Figure 14 presents the influence of the Hartmann number on the local Nusselt number for $P_e = 100$and $B_r = 0$, considering four values of $H_a = 1,5,50,$and 100. Overall, all curves exhibit a similar qualitative behavior. However, the local Nusselt number $N_u$increases as the Hartmann number rises, with a tendency toward saturation observed around $H_a = 50$. This indicates that the intensity of heat transfer between the fluid and the channel walls is enhanced by stronger magnetic effects.
In the entrance region, the local Nusselt number shows a sharp decline, and this decrease becomes more significant when the Hartmann number increases. Further downstream, in the thermally fully developed region (for sufficiently large ξ), the local Nusselt number

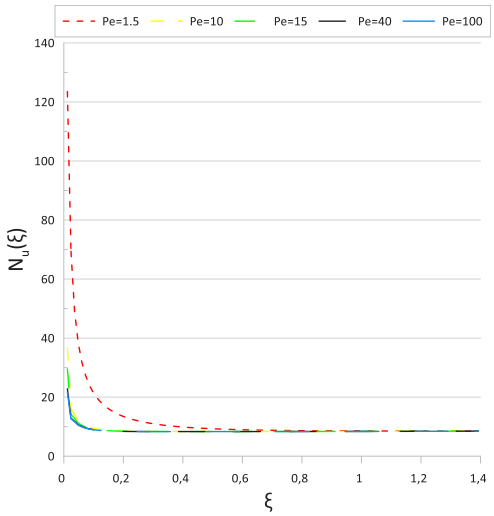

Figure 15: Distribution of local Nusselt number for $H_a = 5\ and\ B_r = 0$

approaches a constant asymptotic value, which remains dependent on the Hartmann number.

The case of the local Nusselt number N_u for $H_a = 5$, $B_r = 0$ and $P_e = 1.5, 10, 15, 40$ and 100 is depicted in Figure 15. Here as well, it is shown that all the curves generally maintain the same shape. We observe that N_u increases more significantly for smaller Peclet numbers as we approach the inlet section. Physically, this is explained by the fact that the thermal boundary layer develops more rapidly for smaller values of P_e [6]. For values of $P_e \geq 10$, it is observed that P_e has a very slight influence on N_u and all the curves become indistinguishable for sufficiently large ξ.

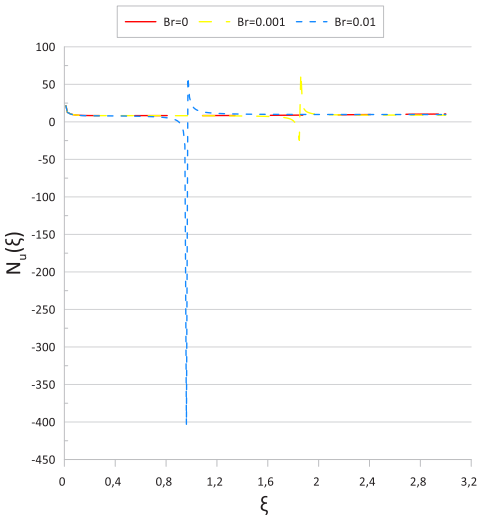

Figure 16: Distribution of local Nusselt number for $P_e = 100$ *and* $H_a = 5$

Figure 16 illustrates the effect of the Brinkman number on the local Nusselt number for $P_e = 100$ and $H_a = 5$ with three values of B_r: $B_r = 0, 0.001$ and 0.01. It is observed that all the curves overlap for the chosen values of B_r indicating that the effect on N_u is very weak in this case. Additionally, for non-zero values of B_r singularities arise due to the vanishing of the denominator, i.e., the term $\theta_w - \theta_b$, as shown in Figure 17 This figure depicts the local Nusselt number and the denominator of N_u, $\theta_w - \theta_b$ for $B_r = 0.01, H_a = 5$ and $P_e = 100$. It is clear from this figure that the singularity occurs when the term $\theta_w - \theta_b$ vanishes, i.e., when the mean temperature of the mixture equals the wall temperature before exceeding it due to heating by dissipation.

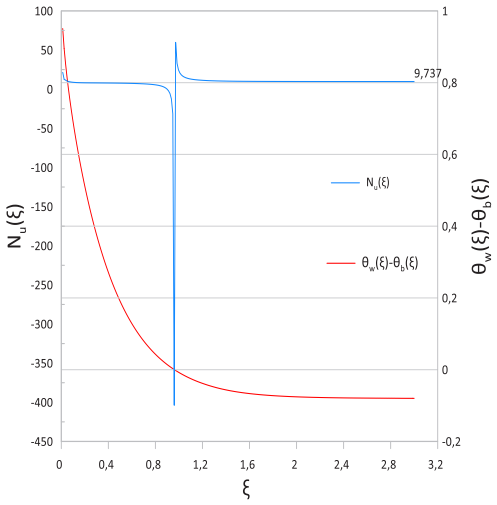

Figure 17: Distribution of $\theta_w - \theta_b$ and the local Nusselt number for $P_e = 100, H_a = 5\ and\ B_r = 0.01$

4.1 Application

Two examples are presented in Figures Figure 18 and Figure 19 to study the effect of the magnetic field on the radial temperature profile $(°C)$ with an axial distance $x(m)$. The objective of these examples is to study the effect of the magnetic field on high-temperature liquid metals in laminar flow, in both cases of heating and cooling, for sodium and lithium liquids.

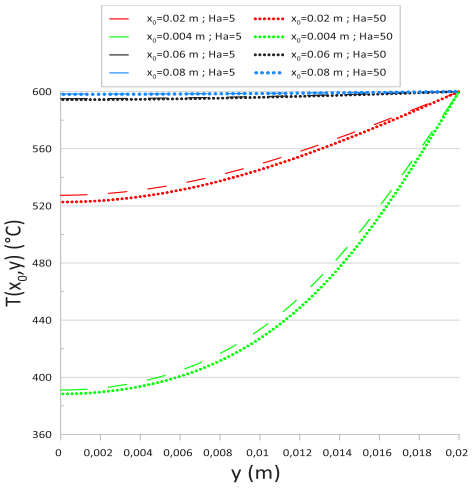

Figure 18: Radial temperature profiles for sodium liquid for $P_e = 5$, for various axial distances x and Hartmann numbers H_a.

In the case of liquid sodium heating Figure 18, at $T_i = 365\ °C$ and $T_w = 600\ °C$, with physical properties [15] given at the mean temperature $T_m = \frac{T_w + T_i}{2} = 482.5\ °C$ $\rho = 838.3\ kg/m^3$, $\mu = 2.43 \times 10^{-3} kg/ms$, $k = 66.88\ W/m°C$, $\alpha = 63.1 \times 10^{-6}\ m^2/s$, $P_r = 0.0046$ (where P_r is the Prandtl number), $R_e = 1087$ (where R_e is the Reynolds number), $P_e = P_r\ R_e = 5$, $b = 2\ cm$ with $U_m = 0.16\ m/s$ and $B_r = 3.95 \times 10^{-9}$. It is noted that increasing x leads to an increase in temperature until reaching a radial profile that no longer varies with y for a value of $x = 8\ cm$. Moreover, it is observed that increasing the magnetic field decreases the temperature, but the effect of the magnetic field becomes negligible for a value of $x = 6\ cm$. In the case of liquid lithium cooling Figure 19 at $T_i = 427\ °C$ and $T_w = 316\ °C$, $\rho = 493.9\ kg/m^3$, $\mu = 4.2 \times 10^{-4} kg/ms$, $k = 40.66\ W/m°C$, $\alpha = 19.48 \times 10^{-6}\ m^2/s$, $P_r = 0.04375$, $R_e = 2286$, $P_e = 100$, $b = 1\ cm$ with $U_m = 0.19\ m/s$ and $B_r = 1.6 \times 10^{-9}$. It is observed that the temperature decreases with increasing x until reaching a radial profile that no longer varies with y for a value of $x = 1.5\ m$ Furthermore, it is noted that increasing the magnetic field increases the temperature up to a value of $x = 0.9\ m$ where the effect of the magnetic field becomes negligible. In liquid metals, the Brinkman number is very small [1]. In the case of heating, the magnetic field decreases the temperature, which is the opposite of what happens in the case of cooling.

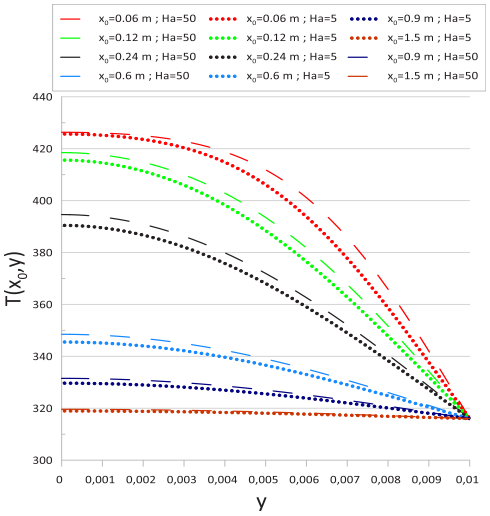

Figure 19: Radial temperature profiles for lithium liquid for $P_e = 100$, for various axial distances x and Hartmann numbers H_a.

Conclusion

This study presents a numerical investigation of laminar Hartmann flow in a channel formed by two parallel plates, subjected to a uniform transverse magnetic field and maintained at constant wall temperature conditions. The model accounts for axial thermal conduction as well as both viscous and Joule dissipation effects. The governing equations are solved using the implicit Alternating Direction Splines (SADI) method,

which is based on cubic spline interpolation. This approach ensures high numerical accuracy, good stability properties, and allows the use of relatively coarse meshes, leading to rapid convergence of the solution.

The temperature distribution and the Nusselt number are analyzed as functions of the Peclet, Hartmann, and Brinkman numbers. The obtained results indicate that, when viscous dissipation is neglected ($B_r = 0$), both the Nusselt number and the mean temperature decrease as the Hartmann number increases. In contrast, when viscous dissipation is taken into account ($B_r \neq 0$), both quantities increase with increasing Hartmann number. Moreover, it is observed that higher values of the Peclet and Brinkman numbers lead to an increase in both the Nusselt number and the average temperature.

Appendix A

We have:

$$\frac{\partial\theta(\xi,\eta)}{\partial\xi} = K_1 \tag{A. 1}$$

Where K_1 is a constant to be determined. The asymptotic solution for $\xi \approx 0$ $negative$ can be written in the following form:

$$\theta(\xi,\eta) = f(\xi) + g(\eta) \tag{A. 2}$$

Substituting equation (A. 2) into equation (3), and integrating both sides of the equality between 0 and 1, and knowing that $\left.\frac{\partial\theta(\xi,\eta,\tau)}{\partial\eta}\right|_{\eta=1} = 0$ for $\xi < 0$, we find:

$$K_1 = \frac{B_r \int_0^1 ([H_a^2 U(\eta)^2 + \left[\frac{dU(\eta)}{d\eta}\right]^2)d\eta}{\int_0^1 U(\eta)d\eta} \tag{A. 3}$$

Thus :

$$K_1 = \frac{B_r\, H_a^2\, ch(H_a)}{ch(H_a) - 1} \tag{A. 4}$$

For the function $g(\eta)$, substituting equation (A. 2) into equation (3) yields:

$$g''(\eta) = K_1 U(\eta) - R(\eta)$$

Integrating twice with respect to η, we obtain:

$$\begin{aligned} g(\eta) = {} & \frac{\frac{ch(H_a)}{2}\eta^2 - \frac{ch(H_a)}{H_a^2}}{(ch(H_a)-1)^2} K_1 \\ & - \frac{B_r H_a^2}{(ch(H_a)-1)^2}\left[\frac{ch(H_a)^2\eta^2}{2} - \frac{2\, ch(H_a)\, ch(H_a\eta)}{H_a^2}\right. \\ & \left. - \frac{ch(H_a\eta)^2}{2H_a^2}\right] + C \end{aligned} \tag{A. 5}$$

From equations (A. 1) and (A. 2) :

$$f(\xi) = K_1\xi + K_2 \tag{A. 6}$$

Thus, it remains to determine the constant $D = C + K_2$ **.** For this, we use the condition $\theta(0,1) = 0$ and find:

$$D = \frac{-B_r H_a^2}{(ch(H_a)-1)^2}\left[\frac{ch(H_a)^2}{H_a^2} + \frac{ch(H_a)^2}{2H_a^2}\right] \tag{A. 7}$$

Therefore :

$$\theta(\xi,\eta) = K_1\xi + \frac{\frac{ch(H_a)}{2}\eta^2 - \frac{ch(H_a)}{H_a^2}}{(ch(H_a)-1)^2}K_1 - \frac{B_r H_a^2}{(ch(H_a)-1)^2}\left[\frac{ch(H_a)^2\eta^2}{2} - \frac{2\,ch(H_a)\,ch(H_a\eta)}{H_a^2} - \frac{ch(H_a\eta)^2}{2H_a^2}\right] + \frac{-B_r H_a^2}{(ch(H_a)-1)^2}\left[\frac{ch(H_a)^2}{H_a^2} + \frac{ch(H_a)^2}{2H_a^2}\right] \quad \text{(A. 8)}$$

Nomenclature

b	Separation distance halfway between the walls (m)
B_0	Magnetic field $(Tesla)$
B_r	Brinkman number
c_p	Specific heat capacity $(J.Kg^{-1}.K^{-1})$
H_a	Nombre de Hartman
i, j	Longitudinal and transverse index
k	Thermal conductivity $(W.m^{-1}.K^{-1})$
N_u	Nusselt number
P_e	Peclet number
t	Time (s)
T	Temperature (K)
T_b	Mean temperature (K)
u	Longitudinal velocity $(m.s^{-1})$
U	Dimensionless velocity
U_m	Maximum velocity $(m.s^{-1})$
x	Longitudinal coordinate
y	Transverse coordinate
Greek symbols	
ξ	Dimensionless axial position
η	Dimensionless radial position
θ	Dimensionless temperature
ρ	Density of the fluid $(kg.m^{-3})$
μ	Dynamic viscosity $(Pa.s)$

References

1. J. Lahjomri, A. Oubarra, A. Alemany, *Heat transfer by laminar Hartmann flow in thermal entrance region with a step change in wall temperatures: the Graetz problem extended*, Int. J. Heat Mass Transf. **45**, 1127–1148 (2002).
2. S. Aïboud-Saouli, N. Settou, S. Saouli, N. Meza, *Second-law analysis of laminar fluid flow in a heated channel with hydromagnetic and viscous dissipation effects*, Appl. Energy **84**, 279–289 (2007).
3. K.V.S. Raju, T. Sudhakar Reddy, M.C. Raju, P.V. Satya Narayana, S. Venkataramana, *MHD convective flow through porous medium in a horizontal channel with viscous dissipation and Joule heating*, Ain Shams Eng. J. **5**, 543–551 (2014).
4. S. Selimli, Z. Recebli, E. Arcaklioglu, *MHD numerical analyses of hydrodynamically developing laminar liquid lithium duct flow*, Int. J. Hydrogen Energy **40**, 15358–15364 (2015).
5. Michiyoshi, R. Matsumoto, *Heat transfer by Hartmann's flow in thermal entrance region*, Int. J. Heat Mass Transf. **7**, 101–112 (1964).
6. J. Lahjomri, K. Zniber, A. Oubarra, A. Alemany, *Heat transfer by laminar Hartmann's flow with uniform wall heat flux: the Graetz problem extended*, Energy Convers. Manag. **44**, 11–34 (2003).
7. K. Zniber, A. Oubarra, J. Lahjomri, *Analytical solution of heat transfer in MHD flow with sinusoidal wall heat flux*, Energy Convers. Manag. **46**, 1147–1163 (2005).
8. M.E. Sayed Ahmed, *Numerical solution of power-law fluid flow and heat transfer with magnetic field in a rectangular duct*, Int. Commun. Heat Mass Transf. **33**, 1165–1176 (2006).
9. H. Ragueb, A. Tahiri, D. Behnous, B. Manser, K. Rachedi, K. Mansouri, *Irreversibilities and heat transfer in MHD microchannel flow under differential heating*, Int. Commun. Heat Mass Transf. **149**, 106979 (2023).
10. S. Elalaoui, A. Oubarra, J. Lahjomri, K. Zniber, *Heat transfer in thermal entrance region of a wavy conduit*, Comput. Therm. Sci. **15**, 2023.
11. P. Kumar, G.M.N. Guruprasad, F. Almeida, Y. El Khatib, Q. Al-Mdallal, *Entropy optimization of micropolar nanofluid flow in porous microchannel*, Int. J. Thermofluids **30**, 101428 (2025). https://doi.org/10.1016/j.ijft.2025.101428
12. M.M. Bhatti, L. Phali, C.M. Khalique, *Heat transfer in electro-magnetohydrodynamic Carreau fluid between micro-plates*, Arch. Appl. Mech. **91**, 1683–1695 (2021).
13. P. Wang, R. Kahawita, *Numerical integration of PDEs using cubic splines*, Int. J. Comput. Math. **13**, 271–286 (1983).
14. F.V. Castellões, J.N.N. Quaresma, R.M. Cotta, *Convective heat transfer enhancement in low Reynolds number flows with wavy walls*, Int. J. Heat Mass Transf. **53**, 2022–2034 (2010).
15. M.N. Özisik, *Heat Transfer: A Basic Approach*, McGraw-Hill, New York (1985).